

## Classical description of threshold effects in ion–atom ionization collisions

J Fiol†, C Courbin‡, V D Rodríguez§|| and R O Barrachina†||

† Centro Atómico Bariloche and Instituto Balseiro¶, 8400 S C de Bariloche, Río Negro, Argentina.

‡ Laboratoire de Dynamique des Ions, Atomes et Molécules, Université P et M Curie, 4 Place Jussieu, T12-B75, F-75 252 Paris Cedex 05, France

§ Departamento de Física, Facultad de Ciencias Exactas y Naturales, Universidad de Buenos Aires, 1428 Buenos Aires, Argentina

Received 9 August 2000, in final form 2 October 2000

**Abstract.** We employ a three-body classical trajectory Monte Carlo (CTMC) method to calculate the recoil-ion momentum distribution at its kinematic threshold in ion–atom ionization collisions. We analyse how this threshold is intertwined by dynamical constraints to the *electron capture to the continuum* cusp in the electron double differential cross section. We compare these calculations with those from a full quantum-mechanical description and explore how these structures depend on the interactions among the three particles in the final state.

### 1. Introduction

For many decades, research in ion–atom ionization collisions was mainly devoted to total cross sections or to the energy and angular distributions of the ejected electrons. In particular, 30 years ago, one of the first measurements of the electron double differential cross section revealed an effect which became the focus of a large amount of experimental and theoretical research. This was the appearance of a sharp cusp-shaped peak when the electron velocity matches that of the projectile in the forward direction (Crooks and Rudd 1970). More recently, the unexpected observation of cusp electrons in coincidence with neutral H and He projectiles (Sarkadi *et al* 1989, Penent *et al* 1991) provoked a renewed wave of interest in the subject.

On the other hand, recent improvements in the cold-target recoil-ion momentum (COLTRIM) spectroscopy technique have opened up the additional possibility of measuring the momentum distribution of the recoiling target ion (Dörner *et al* 1995a, 2000, Ullrich *et al* 1997). Until recently, measurements of this distribution had failed to show any kind of structure as conspicuous as the just mentioned ‘electron capture to the continuum’ (ECC) peak in the electron double differential cross section (DDCS). However, a threshold structure in the longitudinal recoil-ion momentum was predicted some years ago (Rodríguez *et al* 1995) and shown to be associated with this same ECC cusp in the electron momentum distribution (Rodríguez *et al* 1995, Rodríguez and Barrachina 1996). Recent measurements by Weber *et al* (2000) have demonstrated this structure in swift proton–helium collisions.

|| Also member of the Consejo Nacional de Investigaciones Científicas y Técnicas, Argentina.

¶ Comisión Nacional de Energía Atómica and Universidad Nacional de Cuyo, Argentina

The relation between the recoil-ion kinematic threshold and the ECC cusp represents a particular case of a deeper and more general structure, where the single-particle kinematics of a three-body continuum are related among themselves by momentum and energy conservation (Barrachina *et al* 2000). In particular, the energy conservation law imposes a limit to the values that the different momenta can attain. Thus, one momentum will reach its maximum value whenever another complementary momentum is zero. The behaviour of the corresponding cross sections will be intertwined in this limit.

Note that this kind of relation among DDCSs only depends on energy and momentum conservation rules and symmetry relations, but not on any particular theoretical model employed for describing the collision dynamics, whether it be classical or quantum-mechanical. Furthermore, the shape of the cusp itself for a Coulomb electron–projectile interaction is known to be correctly described by a classical model (Reinhold and Olson 1989). Thus, this effect represents an excellent *tour de force* for the CTMC method. In particular, this paper shows that this classical approach can be very useful for analysing the basic features of the threshold structure and its relation with the ECC cusp.

The paper is organized as follows. In the next section we briefly review the basic features of the CTMC computational technique. This method is applied to evaluate the behaviour of the recoil-ion momentum (RIM) distribution at its kinematic threshold in an ion–atom ionization collision at intermediate energies. We show how this effect is related to the momentum dependence of the electron DDCS at the ECC cusp. Finally, we discuss the relation of these threshold and cusp effects with the presence of highly excited bound orbitals for the electron–projectile final-state interaction.

## 2. Computational procedure

We investigate the three-body dynamical problem that involves an ion of charge  $Z_P$ , mass  $M_P$  and velocity  $v$  (impulse  $P = M_P v$ ) colliding with a hydrogenic atom of mass  $M_T + m$  in its ground state. The total energy of the colliding system is given by  $E_{\text{Lab}} = M_P v^2/2 + \varepsilon_i$ . By extracting the constant energy  $M v_{\text{CM}}^2/2$  associated with the movement with velocity  $v_{\text{CM}} = M_P v/M$  of the whole system of mass  $M = M_T + M_P + m$ , we obtain the energy in the centre-of-mass reference frame  $E_i = \mu_T v^2/2 + \varepsilon_i$ . Here  $\mu_T = (m + M_T)M_P/M$  is the reduced mass of the initial projectile–target configuration. We evaluate the three-body dynamics by means of a classical trajectory Monte Carlo (CTMC) method that is similar to those used in previous works (Lewartowski and Courbin 1992) and by other authors (Abrines and Percival 1966, Olson and Salop 1977, Cohen 1982, Reinhold and Olson 1989). Hamilton’s canonical equations in the centre-of-mass reference system are solved numerically for a large number of trajectories by means of a modified middle-point code with adaptive step-size control (Bulirsch and Stoer 1966).

The randomly chosen initial conditions are characterized by the impact parameter  $b$ , and a Kepler orbit of energy  $\varepsilon_i = -0.5$  au for the target electron. This orbit is specified by the eccentricity, three Euler angles fixing the orbital plane and orientation randomly in space and an eccentric angle that defines the initial position of the electron along this orbit (Bandarage and Parson 1990). The square of the impact parameter is randomly chosen with uniform density within a range  $0 \leq b^2 \leq b_{\text{max}}^2$  beyond which ionization is negligible. The equations of motion are integrated until the recoil-ion momentum converges and the excitation, charge-transfer and ionization channels can be neatly separated according to energy criteria (Lewartowski and Courbin 1992).

In principle, the final configuration of the ionization channel is characterized by the final momenta of the electron, the (recoil) target ion and the projectile in the laboratory reference

frame,  $\mathbf{k}$ ,  $\mathbf{K}_R$  and  $\mathbf{K}$ , respectively. However, from energy and momentum conservation, these quantities are not independent. In particular, the momentum conservation law,  $\mathbf{k} + \mathbf{K}_R + \mathbf{K} = \mathbf{P}$ , provides a trivial reduction by three of the number of parameters that characterize the final scattering state. Thus, the final state of the three-body system can be described in terms of two independent momenta, the customary  $\mathbf{k}$  and the momentum transfer  $\mathbf{Q} = \mathbf{P} - \mathbf{K}$ , such that  $\mathbf{K}_R = \mathbf{Q} - \mathbf{k}$ .

Switching back to the centre-of-mass reference system, we describe the final three-body kinematics using a set of Jacobi coordinates,  $\mathbf{r}_p$  and  $\mathbf{R}_p$ , that locates the electron relative to the projectile P and the centre of mass of the electron–projectile system relative to the recoiling target ion (Macek and Shakeshaft 1980). In momentum space, the final state of the system in the ionization channel is described by the associated pair  $(\mathbf{k}_p, \mathbf{K}_p)$ . The final kinetic energy of the three-body system can be written as

$$E_f = \frac{1}{2m_p} k_p^2 + \frac{1}{2\mu_p} K_p^2$$

where  $m_p = mM_p/(m + M_p)$  and  $\mu_p = (m + M_p)M_T/M$  are the reduced masses of the rearrangement channel. The differential cross section for the ionization collision can be written in terms of these Jacobi impulses (atomic units are used throughout),

$$\frac{d\sigma}{d\mathbf{k} d\mathbf{Q} d\mathbf{K}_R} = \delta(\mathbf{k} - \mathbf{Q} + \mathbf{K}_R) \frac{d\sigma}{d\mathbf{k}_p d\mathbf{K}_p}.$$

In particular, since  $\mathbf{K}_R = M_T \mathbf{v}_{CM} - \mathbf{K}_p$ , the double differential cross section in the recoil-ion momentum reads

$$\frac{d\sigma}{d\mathbf{K}_R} = \frac{d\sigma}{d\mathbf{K}_p} = \int \frac{d\sigma}{d\mathbf{k}_p d\mathbf{K}_p} d\mathbf{k}_p.$$

We calculate this cross section using the following formula:

$$\frac{d\sigma}{d\mathbf{K}_R} = \frac{\pi b_{\max}^2}{N} \frac{N_i}{\Delta \mathbf{K}_R}$$

where  $N$  is the total number of trajectories with the impact parameter in the range  $(0, b_{\max})$ .  $N_i$  spans those trajectories for which the energy criterion for ionization is fulfilled and the recoil-ion momentum ends within the range  $\Delta \mathbf{K}_R$ .

From earlier CTMC works on the ECC peak by proton impact (Bandarage and Parson 1990, Reinhold and Olson 1989) it is known that the electron DDSCS  $d\sigma/d\mathbf{k}$  converges so slowly that it is necessary to extend the integration of the equations of motion over distances of the order of  $10^6$  au. In this paper, however, the distance of convergence is reduced to hundreds of atomic units, since the recoil-ion spectra are much less sensitive than the momentum distributions of the much lighter and mobile electrons.

### 3. Kinematical threshold

The energy conservation law,  $E_i = k_p^2/2m_p + K_p^2/2\mu_p$ , imposes a limit on the values that the impulse  $K_p$  can attain. Thus,  $K_p$  reaches its maximum value

$$K_p^{\max} = \sqrt{2\mu_p E_i}$$

whenever  $k_p = 0$ . Therefore,  $\mathbf{K}_R$  remains within a sphere in momentum space

$$|\mathbf{K}_R - M_T \mathbf{v}_{CM}| \leq \sqrt{\mu_p \mu_T} v \sqrt{1 - \frac{|\varepsilon_i|}{\mu_T v^2/2}} \quad (1)$$

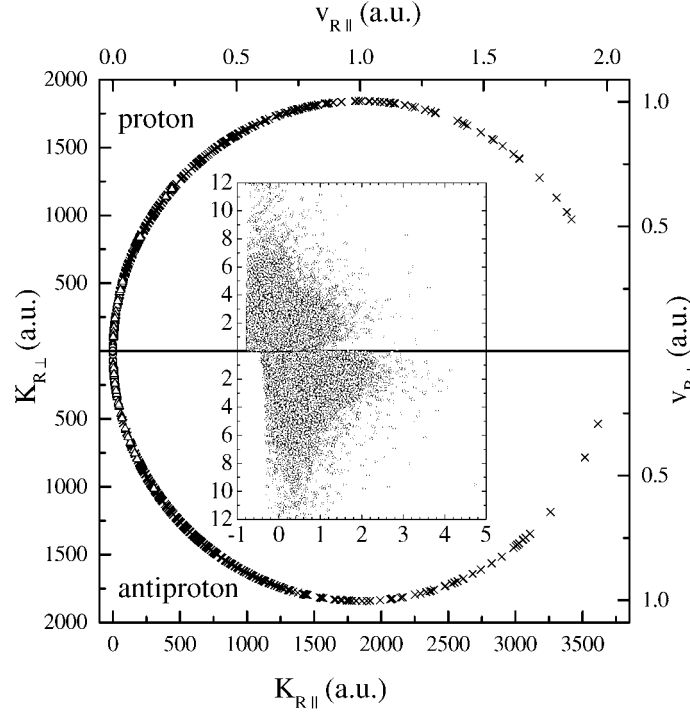


**Figure 1.** By energy conservation, the momentum  $\mathbf{K}_R$  of the receding target ion T, in an ionization process, remains within a sphere in momentum space, whose surface corresponds to zero relative projectile-electron energy. The data correspond to the ionization of hydrogen atoms by the impact of 100 keV protons (upper part) and antiprotons (lower part). The inset zooms in on the threshold region for the target recoiling with small momentum.  $2 \times 10^6$  trajectories amount to the spot near the origin ( $\circ$ ). Since the cross section decreases very fast with increasing momentum  $\mathbf{K}_R$ , we employed an incoming flux 40 times larger with  $b < 0.01$  au ( $\Delta$ ) and 8000 times larger with  $b < 0.001$  au ( $\times$ ) to fill the rest of the sphere in momentum space.

as shown in figure 1 for the ionization of atomic hydrogen by 100 keV protons (projectile velocity  $v \approx 2$  au). We also quote results for antiproton impact at the same energy. Two aspects of these results merit some further clarification: firstly, even though  $\mathbf{K}_R$  seems to lie ‘on’ a sphere in momentum space centred at  $\mathbf{K}_R \approx m_N \mathbf{v}$  ( $m_N = M_T M_P / (M_T + M_P)$ ) and with radius  $K_P^{\max}$ , a closer look shows that it is actually ‘within’ this sphere, but extremely close to its surface. In fact, any ionization process where the electron is emitted with a relative electron–projectile velocity smaller than  $v$ , i.e. within the binary encounter circle, will end up with  $\mathbf{K}_R$  on a thin layer with a thickness of the order of  $m_P K_P^{\max} / 2\mu_T$  ( $\approx K_P^{\max} \times 10^{-5} / 2$ , for a proton–hydrogen collision), just below the surface of the sphere.

Secondly, the cross section  $d\sigma/dK_R$  decreases very quickly with increasing momentum  $\mathbf{K}_R$ , and is strongly confined within a small region around the origin. Larger values of  $\mathbf{K}_R$  correspond to very small impact parameters. This is clearly seen in figure 2, where the angle  $\theta_R$  of the recoil ion, measured from the backwards direction in the centre-of-mass reference frame, is displayed versus the impact parameter  $b$ , for the ionization of hydrogen atoms by the impact of 100 keV protons. For an elastic ion–ion collision,  $\theta_R$  is equal to the deflection angle  $\theta_P$  of the projectile in the centre-of-mass reference frame, and the data actually resemble the corresponding dispersion relation  $b = (Z_P Z_T / m_N v^2) \cot(\theta_P / 2)$ . However, there is a strong

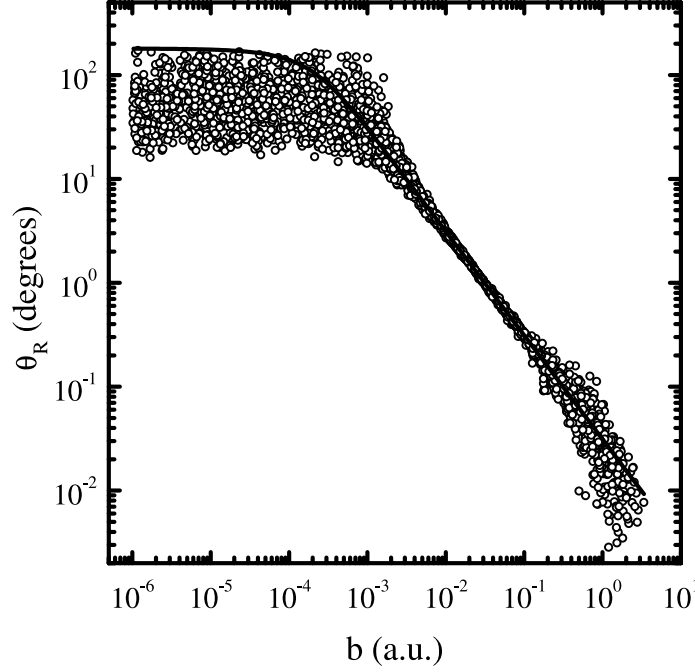


**Figure 2.** Angle  $\theta_R$  of the recoil ion measured from the backwards direction in the centre-of-mass reference frame and displayed versus the impact parameter  $b$ , for the ionization of hydrogen atoms by the impact of 100 keV protons. The full curve represents the dispersion relation  $\theta_R = \theta_R(b)$  for an elastic proton–proton collision.

deviation from this curve when  $b$  is smaller than approximately  $10^{-3}$ , due to the motion of the proton orbiting around the centre of mass of the target atom in the initial state. Note that in order to observe these very rare collision events, the impact parameters have been uniformly distributed on a logarithmic scale in figure 2. Similarly, we increased the incoming flux of projectiles with small impact parameters ( $b < 0.01$  au) in figure 1.

The inset in figure 1 shows a close-up of the RIM distribution in the backward direction for the cases of proton and antiproton impact. The kinematic threshold given by (1) is clearly observed. Beyond it, the ionization cross section is exactly zero. The different ways in which this limit is reached are illustrated in this inset. We can observe that for proton impacts the DDCS reaches a finite value at threshold. On the other hand, the RIM distribution for antiprotons decreases to zero as  $K_R$  approaches the threshold. These threshold behaviours are neatly visible in figure 3 for the longitudinal recoil-ion momentum distribution

$$\frac{d\sigma}{dK_{R\parallel}} = \int \frac{d\sigma}{dK_P} dK_{P\perp}. \quad (2)$$

Here  $K_{P\perp} = -K_{R\perp}$  is the projection of  $K_P$  onto a direction perpendicular to  $v$ . Note that for the case of proton impact, the longitudinal recoil-ion momentum cross section does not vanish smoothly, but presents a sharp discontinuity that increases for smaller impact energies. Furthermore, it is displaced towards the backwards direction, while the opposite behaviour is observed for antiproton impact (Wood and Olson 1996). The maximum in the longitudinal RIM distribution corresponds to the emission of low-energy electrons. However, for proton and antiproton impact, it is evidently shifted to values lower or higher, respectively, than the

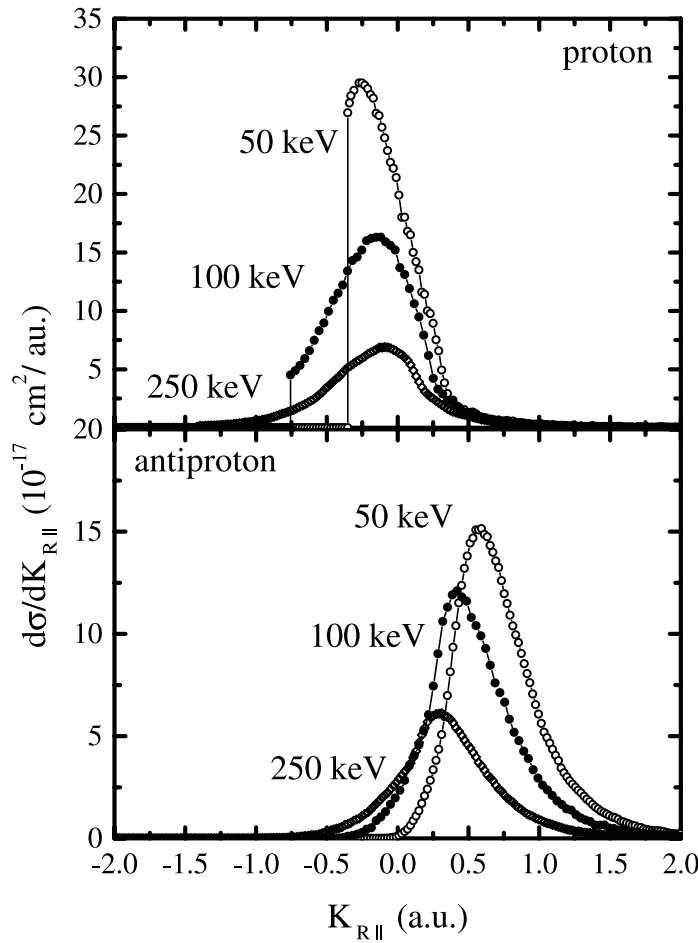


**Figure 3.** Parallel momentum distribution of the receding target ion T, for the ionization of hydrogen by 50 (○), 100 (●), 250 (◇) keV proton and antiproton impact.

position  $K_{R||} = |\varepsilon_i|/v$  which corresponds to electrons emitted with zero energy. This effect is due to the well known asymmetry of the low-energy peak in the electron distribution (Wang *et al* 1996).

In figure 4 we compare our CTMC calculation of the longitudinal recoil-ion momentum distribution for the ionization of helium by 100 and 250 keV proton impact with experimental results by Dörner *et al* (1995a) and a continuum distorted wave–eikonal initial-state (CDW-EIS) calculation. An independent-electron model was employed in both the CTMC, as done by Schulz and Olson (1988) and CDW-EIS calculations (Rodríguez *et al* 1995). They have similar shapes and agree in magnitude between themselves and with the experimental data at 250 keV, even though the maximum of the CTMC distribution shows an appreciable shift towards lower momenta. This consistent backward shift of the CTMC calculation with respect to CDW-EIS has already been reported by other authors (Tribedi *et al* 1996, Wood and Olson 1996, Wang *et al* 1996).

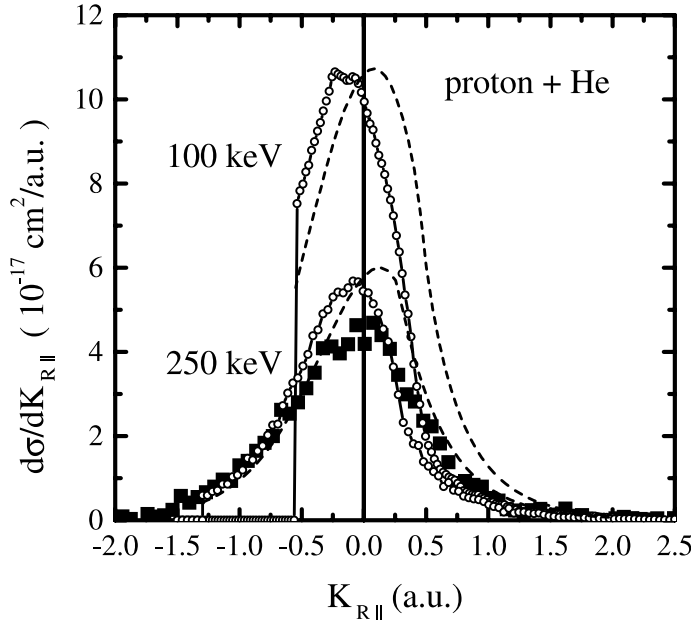


**Figure 4.** Parallel momentum distribution of the receding target ion T, for the ionization of helium by 100 and 250 keV proton impact. The CTMC results (○) are compared with experimental data by Dörner *et al* (1995) for 250 keV (■), and with quantum mechanical CDW-EIS calculations (---).

#### 4. Relation with the ECC process

Since the  $K_p \rightarrow K_p^{\max} = \sqrt{2\mu_p E_i}$  limit occurs when  $k_p \rightarrow 0$ , it is clear that the conspicuous discontinuity in the RIM distribution for proton impact in figures 1, 3 and 4 has to be related to the structure of the ECC cusp in  $d\sigma/dk_p$ , i.e. to a mechanism where an electron initially bound to the target atom ends up in a low-lying continuum state of the charged projectile. Strangely enough, this simple relation had been overlooked in previous studies of cusp formation or threshold effects until recently, when it was demonstrated by Rodríguez *et al* (1995).

The appearance of the threshold and ECC effects in a CTMC calculation can be understood by relying on a classical version of a continuation argument suggested by Rudd and Macek (1972), regarding the relationship between electron capture to Rydberg and continuum states in ion–atom collisions. By momentum conservation, the impulse  $K_R$  acquired by the receding ion in a rearrangement process equals the change in the projectile's momentum after the acquisition of the electron. Furthermore, it is related to the energy  $\varepsilon$  of the bound electron–projectile orbit in the exit channel, by means of the energy conservation law

$$E_i = |K_R - M_T v_{CM}|^2 / 2\mu_p + \varepsilon. \quad (3)$$

The emitted electron might overcome the attraction of the outgoing projectile and reach the detection zone in an asymptotically free trajectory. However, it can also be captured in a bound state of the projectile. These electron-capture contributions make the energy spectrum  $d\sigma/d\varepsilon$  finite for  $\varepsilon \leq 0$ . And, by continuation across the ionization limit, the same happens with the emitted electron momentum distribution

$$\frac{d\sigma}{dk_p^2/2m_p} = m_p k_p \int \frac{d\sigma}{dk_p} d\hat{k}_p$$

in the  $k_p \rightarrow 0$  limit. Thus, in this threshold limit we can write

$$\frac{d\sigma}{dk_p} \approx \frac{A(\hat{k}_p)}{m_p k_p}$$

and the double differential cross section in the Jacobi momentum  $k_p$  presents a  $1/k_p$  divergence at  $k_p = 0$ . This is the same kind of structure obtained in the quantum mechanical final-state interaction theory of cusp formation (Barrachina 1997). In both cases, the appearance of this cusp is related to the presence of a continuum of bound states accumulating at zero energy (Macek 1970). The difference is that while in a classical calculation *any* potential with an attractive region has the capability of producing a  $1/k_p$  cusp, in a quantum-mechanical description this can only occur for long-range attractive interactions not decaying faster than  $-1/r_p^2$  (Barrachina 1997).

From (3), the constancy of  $d\sigma/d\varepsilon$  for  $\varepsilon \leq 0$  indicates that

$$\frac{d\sigma}{dK_p^2/2\mu_p} = \mu_p K_p \int \frac{d\sigma}{d\hat{K}_p} d\hat{K}_p$$

also reaches a constant value in the  $K_p \rightarrow K_p^{\max}$  limit. Thus,  $d\sigma/dK_p$  does not diverge or go to zero, but defines an angle-dependent function

$$\frac{d\sigma}{dK_p} \approx \frac{B(\hat{K}_p)}{\mu_p K_p^{\max}}$$

where  $B(\hat{K}_p)$  is trivially related to  $A(\hat{k}_p)$  by angular integration

$$\int A(\hat{k}_p) d\hat{k}_p = \int B(\hat{K}_p) d\hat{K}_p.$$

## 5. Charge exchange

Beyond the threshold, each value of the recoil-ion momentum  $K_R$  is associated with a rearrangement process where the electron is captured into a Kepler orbit around the projectile with energy

$$\varepsilon = E_i - |\mathbf{K}_R - M_T \mathbf{v}_{CM}|^2 / 2\mu_p \leq 0.$$

We can ‘quantize’ these orbits by a suitable association of principal quantum numbers  $n$  to given ranges of energy  $\varepsilon$ .

For the case under consideration of two particles of relative mass  $m_p$  interacting via a Coulomb potential of charge  $-Z_p$ ,  $n$  can be determined following the procedure of Becker and MacKellar (1984). They define a classical number  $n_c$  related to the binding energy  $\varepsilon$  by

$$n_c = \sqrt{-\frac{m_p Z_p^2}{2\varepsilon}}$$

which corresponds to the principal quantum number  $n$  if:

$$\left[ n \left( n - \frac{1}{2} \right) (n - 1) \right]^{1/3} \leq n_c < \left[ n \left( n + \frac{1}{2} \right) (n + 1) \right]^{1/3}.$$

Thus, for each value of  $n$ ,  $K_R$  remains on the surface of a sphere in momentum space, as shown in figure 5 for a 100 keV charge-exchange collision,  $H^+ + H \rightarrow H(n) + H^+$ . The outermost circles represent the capture of the electron into the ground state of the projectile. The other excited states produce spheres in momentum space that accumulate at the radius



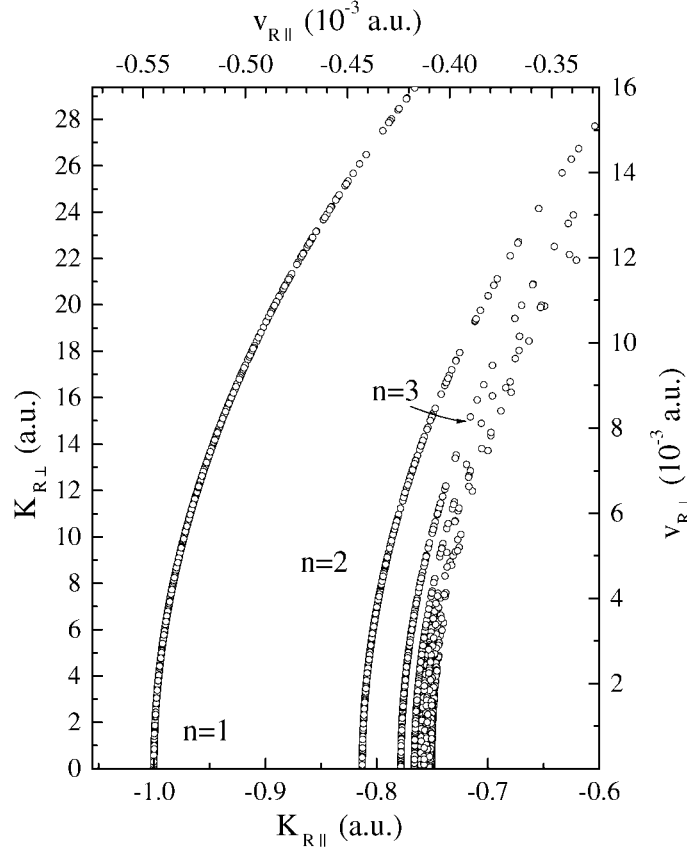


**Figure 5.** In a 100 keV charge-exchange collision,  $H^+ + H \rightarrow H(n) + H^+$ , the recoil-ion momenta  $\mathbf{K}_R$  remain on the surface of spheres characterized by the principal quantum numbers  $n$ . The outermost circle represents the capture of the electron into the ground state of the projectile. The other excited states produce spheres in momentum space that accumulate at the radius  $K_P^{\max} = \sqrt{2\mu_P E_i}$ .

$K_P^{\max}$ . In figure 6 we show the corresponding longitudinal recoil-ion momentum distribution  $d\sigma/dK_{R||}$ , as defined in (2). Note that the different peaks can be clearly resolved for the first values of  $n$  and accumulate towards the ionization threshold  $K_{R||}^{\infty} \approx -v/2 + \varepsilon_i/v$ , as Dörner *et al* (2000) observed experimentally (see also Dörner *et al* 1995b). However, it is important to point out that charge-exchange collisions with  $K_{R||} > K_{R||}^{\infty}$  are not ruled out by energy conservation. They only need to be associated with non-zero values of  $K_{R\perp}$ , so as to keep  $K_P$  larger than  $K_P^{\max}$ . Also note that for each principal quantum number  $n$ , the corresponding RIM distribution shows a strongly asymmetric shape. It vanishes for  $K_{R||}$  smaller than a certain value  $K_{R||}^n \approx -v/2 + (\varepsilon_i - \varepsilon_n)/v$ , and displays a  $(K_{R||} - K_{R||}^n)^{-2}$  tail for  $K_{R||} > K_{R||}^n$ , as shown in the inset. However, it is easy to demonstrate that a simple first-order Born approximation would yield a  $(K_{R||} - K_{R||}^n)^{-6}$  law instead. This difference stems from the description of the final momentum distribution in the classical electron–projectile state.

The RIM distribution relates to the charge-exchange cross sections  $\sigma_n$  by

$$\frac{d\sigma}{dK_P^2/2\mu_P} = \sum_n \sigma_n \delta\left(\frac{K_P^2}{2\mu_P} + \varepsilon_n - E_i\right)$$

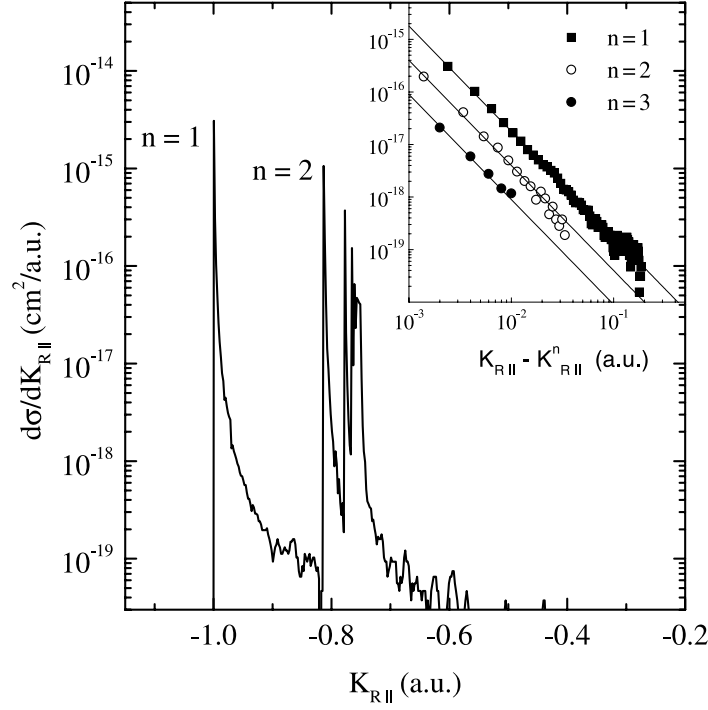


**Figure 6.** Parallel momentum distribution of the receding target ion T, for a 100 keV charge-exchange collision,  $H^+ + H \rightarrow H(n) + H^+$ . The inset displays the shape of the capture peaks compared with the  $(K_{R||} - K_{R||}^n)^{-2}$  behaviour (—).

where, for a Coulomb electron–projectile interaction, the energy spectrum has the form  $\varepsilon_n = -m_p Z_p / 2n^2$ . For capture into a set of high-lying bound states in an energy range near  $\varepsilon_n$  (i.e. principal quantum number close to  $n$ ), this equation yields

$$\left. \frac{d\sigma}{dK_p^2/2\mu_p} \right|_{K_p=\sqrt{2\mu_p(E_i-\varepsilon_n)}} \approx \frac{\sigma_n}{d\varepsilon_n/dn}.$$

As was already shown, this cross section goes to a constant value for  $K_p \rightarrow \sqrt{2\mu_p E_i}$  (this is  $\varepsilon_n \rightarrow 0$  or  $n \rightarrow \infty$ ). Thus we obtain the following scaling rule:

$$\sigma_n \propto \frac{d\varepsilon_n}{dn}.$$

In particular, for an attractive Coulomb final-state interaction,  $\varepsilon_n = -m_p Z_p / 2n^2$  and, therefore,  $\sigma_n$  verifies the well known scaling rule  $\sigma_n \propto 1/n^3$  (Jackson and Schiff 1953), as shown in figure 7 for a 100 keV charge-exchange collision,  $H^+ + H \rightarrow H(n) + H^+$ . It is important to point out that this result does not depend on the dynamical details of the collision, but only on the characteristics of the final-state electron–projectile interaction. Thus the  $1/n^3$  scaling rule applies to any scattering process (excitation or capture) leading to a highly excited bound state by a pure Coulomb potential. Furthermore, in its generalized form, it is valid not only for a Coulomb potential, but for any final-state interaction whose bound states accumulate at zero energy (Barrachina 1997).

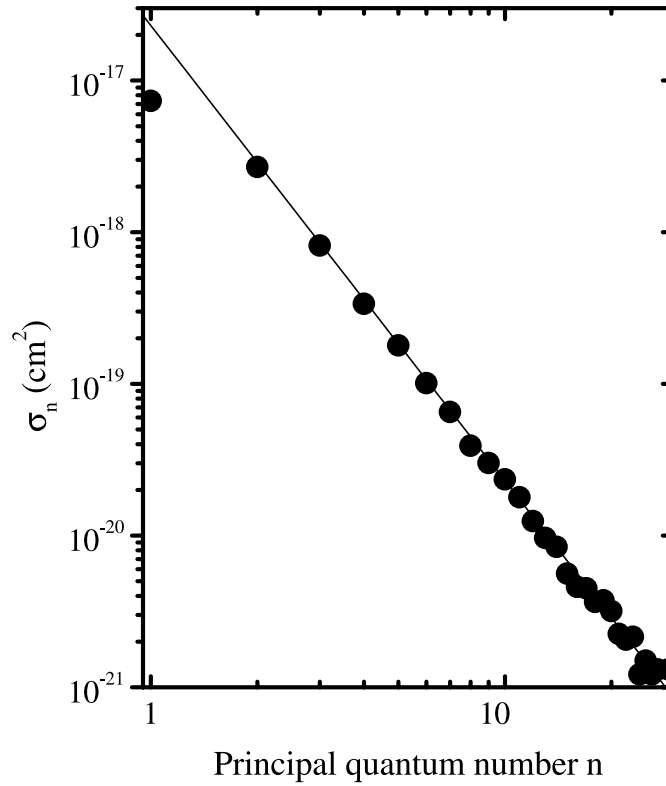


**Figure 7.** Charge-exchange cross sections  $\sigma_n$  as a function of the principal quantum number  $n$  for a 100 keV  $\text{H}^+ + \text{H} \rightarrow \text{H}(n) + \text{H}^+$  collision. The line represents the Jackson-Schiff scaling rule  $\sigma_n \propto 1/n^3$ .

## 6. Conclusions

In this paper we have employed the CTMC method to evaluate the RIM distribution in ion-atom ionization collisions at intermediate energies. We studied its behaviour at the kinematic threshold, discussing its relation with the momentum dependence of the electron DDCS at the ECC cusp, and the presence of highly excited bound orbitals for the electron-projectile final-state interaction. As the presence of a kinematic threshold in the RIM distribution depends only on momentum and energy conservation laws, it occurs in any theoretical description, whether it is classical or quantum mechanical.

It might be surprising that a classical model manages to reproduce the overall behaviour of the cross section at this threshold, since it seems to be a purely quantum mechanical effect related to the analytic properties at zero energy of the regular two-body scattering wavefunctions (Barrachina 1997). Firstly, note that, while its angular dependence, as given by the function  $B(\hat{\mathbf{K}}_p)$ , depends on the actual scattering process, the behaviour of the RIM distribution at the threshold limit does only depend on the characteristics of the final-state interaction between the electron and the projectile. To this end, it does not matter how this particular final-state configuration is reached. In fact, the appearance of a cusp structure both in classical and quantum mechanical models has a common origin. In both cases, the divergence of the electron momentum distribution at  $k_p = 0$  occurs whenever the energy

spectrum of electron–projectile bound states accumulates at zero energy. In this case, by continuity across the ionization limit, the recoil-ion energy distribution  $d\sigma/d(K_P^2/2\mu_P)$  does not vanish at the kinematic threshold. However, while in a classical calculation this occurs with any locally attractive potential, an attractive potential vanishing like  $1/r^2$  or slower at infinity is required in a quantum mechanical description. This explains why CTMC calculations were successful in the description of the ECC process by ionic projectiles (Reinhold and Olson 1989), or even by neutral hydrogen atoms (Tökési *et al* 1997, Sarkadi *et al* 2000). In this latter case, owing to its degeneracy in  $\ell$ , an excited state can acquire a dipole momentum, producing a final-state interaction with a dipolar ‘tail’  $-\alpha/r_P^2$  and an infinite discrete spectrum that accumulates at zero energy. On the other hand, for a short-range potential  $V(r_P)$ , there is a completely different situation. Under very general conditions, the small- $k_P$  behaviour of electron DDCS shows a characteristic Lorentzian shape (Barrachina 1997), that no classical model can possibly reproduce. This occurs in the case of neutral polarizable projectiles, such as, for instance, helium atoms in metastable  $2^1S$  or  $2^3S$  states, where sizeable ECC structures with characteristic Lorentzian shapes have been observed (Báder *et al* 1997, Macri and Barrachina 1998).

### Acknowledgments

This work has been supported by the Agencia Nacional de Promoción Científica y Tecnológica (Contrato de Préstamo BID 802 OC-AR, grant no 03-04021). The calculations were performed using the computing facilities of the Centre de Calcul de Recherche of the University P and M Curie, France and the Parallel computer cluster, Proyecto FOMEC 779/98, Instituto Balseiro, Universidad Nac de Cuyo. We would like to thank Dr R Dörner for providing us with some very useful information and, in particular, the experimental data in figure 4. We are also grateful to Mrs Ann Borsinger for her help with the preparation of the manuscript.

### References

- Abrines R and Percival I C 1966 *Proc. Phys. Soc.* **88** 861
- Báder A, Sarkadi L, Víkor L, Kuzel M, Závodszy P A, Jalowy T, Groeneveld K O, Macri P A and Barrachina R O 1997 *Phys. Rev. A* **55** R14
- Bandarage G and Parson R 1990 *Phys. Rev. A* **41** 5878
- Barrachina R O 1997 *Nucl. Instrum. Methods B* **124** 198
- Barrachina R O, Fiol J, Rodríguez V D and Macri P 2000 *The Physics of Electronic and Atomic Collisions, 21st Int. Conf.* ed Y Itikawa *et al* (New York: American Institute of Physics) p 510
- Becker R L and MacKellar A D 1984 *J. Phys. B: At. Mol. Phys.* **17** 3923
- Bulirsch R and Stoer J 1966 *Num. Math.* **8** 1
- Cohen J S 1982 *Phys. Rev. A* **26** 3008
- Crooks G B and Rudd M E 1970 *Phys. Rev. Lett.* **25** 1599
- Dörner R, Mergel V, Jagutzki O, Spielberger L, Ullrich J, Moshhammer R and Schmidt-Böcking H 2000 *Phys. Rep.* **330** 95
- Dörner R, Mergel V, Zhaoyuan Liu, Ullrich J, Spielberger L, Olson R E and Schmidt-Böcking H 1995a *J. Phys. B: At. Mol. Phys.* **28** 435
- Dörner R *et al* 1995b *The Physics of Electronic and Atomic Collisions (AIP Conf. Proc. 360)* (New York: AIP) p 495
- Jackson J D and Schiff H 1953 *Phys. Rev.* **89** 359
- Lewartowski E and Courbin C 1992 *J. Phys. B: At. Mol. Opt. Phys.* **25** L63
- Macek J H 1970 *Phys. Rev. A* **1** 235
- Macek J H and Shakeshaft R 1980 *Phys. Rev. A* **22** 1441
- Macri P A and Barrachina R O 1998 *J. Phys. B: At. Mol. Opt. Phys.* **31** 1303
- Olson R E and Salop A 1977 *Phys. Rev. A* **16** 531
- Penent F, Grouard J P, Montmagnon J L and Hall R I 1991 *J. Phys. B: At. Mol. Opt. Phys.* **24** 173

- Reinhold C O and Olson R E 1989 *Phys. Rev. A* **39** 3861
- Rodríguez V D and Barrachina R O 1996 *Phys. Rev. A* **53** 3335
- Rodríguez V D, Wang Y D and Lin C D 1995 *Phys. Rev. A* **52** R9
- Rudd M E and Macek J 1972 *Case Stud. At. Phys.* **3** 48
- Sarkadi L, Pálincás J, Kövér Á, Berényi D and Vajnai T 1989 *Phys. Rev. Lett.* **62** 527
- Sarkadi L, Tökési K and Barrachina R O 2000 *J. Phys. B: At. Mol. Opt. Phys.* **33** 847
- Schultz D R and Olson R E 1988 *Phys. Rev. A* **38** 1866
- Tökési K, Sarkadi L and Mukoyama T 1997 *J. Phys. B: At. Mol. Opt. Phys.* **30** L123
- Tribedi L C, Richard P, Wang Y D, Lin C D and Olson R E 1996 *Phys. Rev. Lett.* **77** 3767
- Ullrich J, Moshhammer R, Dörner R, Jagutzki O, Mergel V, Schmidt-Böcking H and Spielberger L 1997 *J. Phys. B: At. Mol. Opt. Phys.* **30** 2917
- Wang Y D, Rodríguez V D, Lin C D, Cocke C L, Kravis S, Abdallah M and Dörner R 1996 *Phys. Rev. A* **53** 3278
- Weber Th *et al* 2000 to be published
- Wood C J and Olson R E 1996 *J. Phys. B: At. Mol. Opt. Phys.* **29** L257